

## FEDSM-ICNMM2010-30221

### ACOUSTICALLY-COUPLED FLOWS IN COAXIAL SIDE BRANCH RESONATORS WITH BLUFF RECTANGULAR SPLITTER PLATES

Alexey Velikorodny

University of Victoria  
 Victoria, BC, Canada  
 asvelikorodny@gmail.com

Peter Oshkai\*

University of Victoria  
 Victoria, BC, Canada  
 poshkai@uvic.ca

#### ABSTRACT

Fully turbulent inflow past symmetrically located side branches mounted in a duct can give rise to pronounced flow oscillations due to coupling between separated shear layers and standing acoustic waves. The acoustically-coupled flows were investigated using digital particle image velocimetry (PIV) in conjunction with unsteady pressure measurements. Global instantaneous, phase- and time-averaged flow images were evaluated to provide insight into the flow physics during flow tone generation. Onset of the locked-on resonant states was characterized in terms of the acoustic pressure amplitude and frequency of the resonant pressure peak. Structure of the acoustic noise source was characterized in terms of patterns of generated acoustic power, which was evaluated by applying the vortex sound theory in conjunction with global quantitative flow imaging and numerical simulation of the acoustic field. In addition to the basic side branch configuration, the effect of bluff rectangular splitter plates located along the centerline of the main duct was investigated. The first mode of the shear layer oscillation was inhibited by the presence of the plates, which resulted in substantial reduction of the amplitude of acoustic pulsations and the strength of the acoustic source.

#### 1. INTRODUCTION

##### 1.1 Overview of flow acoustic coupling

Pipeline systems with symmetrically-located side branches, shown schematically in Fig. 1, are characterized by high-amplitude flow oscillations, as described by Ziada et al. [1], among others.

Flow-acoustic resonance occurs when the frequency of the self-sustained shear layer oscillations matches the resonant acoustic mode of the side branch.

Interaction between the vorticity-bearing component of the flow and the acoustic field, which is defined as the unsteady irrotational component of the velocity field  $\underline{V}$ , results in formation of large-scale vortical structures that are convected across the mouth of the cavity. The energy transfer is described by the vortex sound theory that was developed by Powell [2] and generalized by Howe [3].

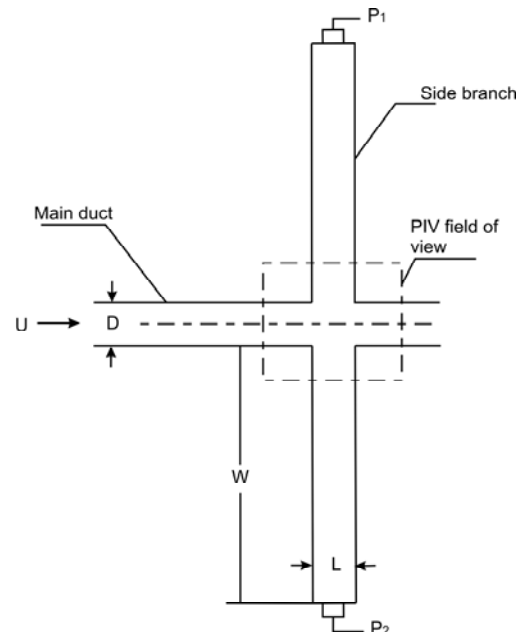


FIG. 1. SCHEMATIC OF THE SIDE BRANCH RESONATOR

Under the assumption of negligible frictional losses, the interaction is described by Crocco's form of Euler's equation

$$\frac{\partial \underline{V}}{\partial t} + \nabla B = -\underline{\omega} \times \underline{V}, \quad (1)$$

\* Direct all correspondence to this author.

where  $B = \int \frac{dp}{\rho} + \frac{1}{2}v^2$  is the total enthalpy (with  $v$  being a potential velocity), and  $\underline{\omega}$  is the vorticity. If the Mach number is small, convective effects on the propagation of acoustic waves can be neglected, and Eqn. (1), upon application of the divergence operator, becomes:

$$\frac{1}{c_0^2} \frac{\partial^2 B}{\partial t^2} - \Delta B = \nabla \cdot (\underline{\omega} \times \underline{V}), \quad (2)$$

where  $c_0$  is the speed of sound. Thus, the source of sound corresponds to the Coriolis force density  $f_c = -\rho_0(\underline{\omega} \times \underline{V})$ , where  $\rho_0$  is the fluid density.

The complex mechanisms of resonant interaction between the acoustic field and the oscillating shear layers in deep cavities and symmetrically located side-branches has been a subject of several experimental investigations [1, 4-10]. At the point of separation, the incident acoustic waves amplify the shear layer fluctuations. The small-scale vortices extract energy from the mean flow to form large-scale vortex structures. The energy of the large-scale vortices, in turn, is transferred into the resonant acoustic field through the vorticity interaction with the downstream corner of the cavity. This mechanism is described in detail by Ziada [7].

## 1.2 Flows over splitter plates

The splitter plates are extensively used in industry to alleviate strong flow-acoustic resonances. Howe [11] theoretically studied the effect of the perforated screens on dissipation of sound in large industrial heat exchangers. Recently, Arthurs et al. [12] investigated the effect of a splitter plate that spans across the entire side branch in order to limit propagation of the acoustic waves. In contrast to the experiments of Arthurs et al. [12], the plates in the present study did not span across the entire side branch, which limited their interference with the acoustic wave propagation.

Flow around a bluff rectangular splitter plate (e.g. Fig 2) was a subject of a number of experimental studies at high Reynolds numbers ( $>20 \cdot 10^3$ ) [13-16]. In these works, the authors accessed the mean and fluctuating characteristics as well as large-scale unsteadiness of turbulent flow around bluff rectangular plates. These studies report characteristic low-frequency flapping of the separated shear layers that form at the leading edges of the plate, which is similar to the absolute instability found in the backward-facing step flows. Strong dependence of this type of flow on turbulence is also well documented. Hillier et al. [17] report shortening of the recirculation zone from  $4.88t$  to  $2.72t$  (where  $t$  is the thickness of the plate) when the free stream turbulence intensity was increased from 1% to 6.5%. A reduction of over 50% in the mean reattachment length ( $X_r$ ) and significant changes in the dynamics of the flow have been demonstrated when turbulence levels reached 12% [16]. These findings are particularly relevant to the present study, since the main results shown in the foregoing sections were obtained with the fully-turbulent inflow at moderate Reynolds numbers.

Direct numerical simulations of flow over a bluff plate at  $Re = 1000$  were performed by Tafti et al. [18]. Although transitional regime was considered, the study reproduced many of the large-scale characteristics observed at higher Reynolds numbers with  $X_r = 6.5t$ . In particular, time-dependent features, such as vortex shedding and vortex convection velocities, were predicted to be in agreement with the aforementioned experiments at high Reynolds numbers. Large-eddy simulation for flows around bluff plate reported

by Suksangpanomrung et al. [19] were performed at  $Re = 50 \cdot 10^3$ . The blockage ratio ( $D/t$ ), where  $D$  is the height of the duct both for the experimental and for the numerical works cited herein was less than 6%.

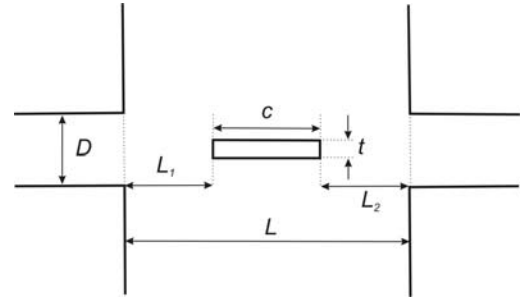


FIG. 2. CLOSE-UP OF THE CROSS-JUNCTION

Separation-reattachment processes are also strongly related to the geometry of the bluff rectangular plate. In particular, an important parameter for the dynamics of the flow structures and vortex street formation is the chord-to-thickness ratio ( $c/t$ ). For  $Re = 8 \cdot 10^3 - 44 \cdot 10^3$  and with the low-turbulence inflow Parker et al. [20] were able to identify four following regimes, which were dependant on the value of  $c/t$ :

1. On short plates ( $c/t < 3.2$ ), flow separation occurs at the leading edge corners, and the shear layers interact directly, without reattaching to the surface of the plate.
2. On longer plates ( $3.2 \leq c/t \leq 7.6$ ), the shear layers reattach to the trailing edge periodically in time. The separation bubbles grow, enveloping the trailing edge of the plate.
3. For still longer plates ( $7.6 < c/t \leq 16$ ), the shear layers always reattach upstream of the trailing edge of the plate and form separation bubbles, which grow and divide in a random manner. This process generates boundary layers with discrete concentrations of vorticity, which move along the plate surface towards the trailing edge.
4. For plates with  $c/t > 16$ , the boundary layers approach fully turbulent state downstream of the leading edge. Thus, flow separation at the trailing edge is not related to the formation of the recirculation zone in the vicinity of the leading edge.

## 2. EXPERIMENTAL SYSTEM AND TECHNIQUES

### 2.1 Experimental system

The flow facility employed in the present study consisted of an inlet plenum chamber, a main duct, and an arrangement of the side branches. The system allowed variations of the channel geometry, optical access to the separated flow area, as well as ability to perform acoustic pressure measurements (as described in Section 2.2). The flow conditioning and the main duct length provided a fully-turbulent inflow in the vicinity of the cross-junction, which was verified experimentally.

The main duct with the width  $D = 6.35$  mm and the side branches with a square cross-sections and the length  $L = 25.4$  mm were utilized in the experiments. The entire system (with the exception of the side branches) was constructed from Plexiglas to allow optical access to the flow. In order to reduce damping and satisfy the necessary resonance condition that occurs in a real pipe-line system, the co-axial side branches were made of a 3.2 mm-thick aluminum. The velocity of air supplied by a compressor was controlled through a system of pressure regulators.

In order to limit the hydrodynamic interaction of the shear layers and to investigate its effect on the intensity of acoustic resonance, a bluff rectangular splitter plate was placed in the middle of the cross-junction (Fig. 2). The flow features were characterized for three cases corresponding to different chord lengths ( $c$ ) of the splitter plates that had a thickness  $t = 1.85$  mm and the out-of plane dimension of 25.4 mm. The three cases corresponded to  $c = 0$  (no splitter plate),  $c = 5$  mm, and  $c = 10$  mm (with chord-to-thickness ratios:  $c/t = 0, 2.7, \text{ and } 5.4$ , respectively). The cases of  $c/t = 2.7$  and  $5.4$  corresponded to the regimes (1) and (2) of the flows around bluff rectangular splitter plates that were described in Section 1.2. In contrast to the earlier studies, a fully-turbulent inflow condition was considered in this work. The dimensions of the cross-junction area are defined in Fig. 2 and summarized in Table 1.

$c$ (mm)	$L_1$ (mm)	$L_2$ (mm)
0	N/A	N/A
5	8.3	12
10	5.3	10

**TABLE 1. CHARACTERISTIC LENGTHS OF SIDE BRANCH RESONATOR WITH SPLITTER PLATE**

## 2.2 Acoustic pressure measurements

Piezoelectric pressure transducers (PCB Model no. 103A02) with a nominal sensitivity 0.21 mV/Pa were used in the experiments. These pressure sensors featured built-in electronics and acceleration compensation. The transducers (indicated as  $P_1$  and  $P_2$  in Fig. 1) were deployed at the closed ends of the side branches.

Acquired pressure signals were transmitted to a National Instruments PXI-4472 data acquisition board with 24-bit resolution and built-in antialiasing capability. The pressure data were acquired at the sampling rate of 8192 Hz. It should be noted that the frequency of interest in the present investigation was equal to 877 Hz, which is approximately 10 times lower than the employed sampling rate. Therefore, at least 10 samples were acquired per acoustic oscillation cycle. The time trace of the pressure signal was employed as a phase reference for the flow imaging according to the procedure described in Section 2.4.

Custom LabView and Matlab codes were employed to process the pressure signals and to characterize them in the frequency domain. The number of samples per data set was calculated according to  $n = f_s / \Delta f$ , where  $f_s$  is sampling rate and  $\Delta f = 0.5$  Hz is frequency resolution.

## 2.3 Quantitative flow imaging

Flow velocity in the cross-junction region was measured using two-component digital PIV. The experimental system is shown schematically in Fig. 3.

Oil droplets with the typical diameter of approximately 1  $\mu\text{m}$  were used as tracer particles. The particles were generated using a LaVision atomizer. The particles were injected into the inlet chamber that was located upstream of the entrance of the main duct. The inlet chamber contained a honeycomb-type flow straightener, which provided uniform inflow into the main duct and also resulted in homogeneous distribution of the seeding particles in the incoming air stream.

A high-speed PIV system was utilized to provide quantitative measurements of the flow in the cross-junction with bluff splitter plates. An Nd:YLF dual cavity pulsed, diode-pumped laser with a maximum energy output of 2 x 25 mJ/pulse and up to 10 kHz repetition rate was used to generate

a planar light sheet that illuminated the flow tracers. The high-speed camera featured a lens with a focal length of 60 mm in conjunction with a 1024 x 1024 pixel CMOS sensor, providing a physical resolution of 30 pixels/mm. The interrogation window size was initially set to 64 x 64 and subsequently reduced to 16 x 16 pixels, which corresponded to the spatial resolution of 5.7 vectors/mm. The system was capable of providing up to 3000 cross-correlated images per second at the full resolution of the camera. The phase of acquisition of each PIV image with respect to a typical acoustic oscillation cycle was obtained by recording the trigger signal to the laser simultaneously with the acoustic pressure signal.

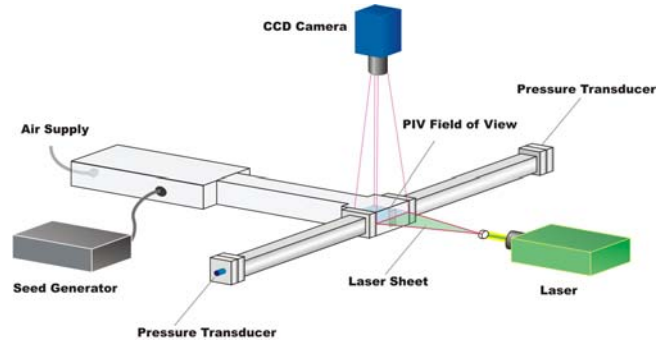


**FIG. 3. SCHEMATIC OF THE EXPERIMENTAL SYSTEM WITH PIV INSTRUMENTATION**

## 2.4 Phase-averaging procedure

The phase of acquisition of each velocity field with respect to a typical acoustic cycle was determined using the trigger signal to the laser, which was recorded together with the acoustic pressure signal.

In contrast to the previous studies, a high framing rate of 1 kHz was utilized in the experiments with bluff splitter plates. At this acquisition frequency, approximately one image pair was acquired during each period of the acoustic oscillation. A typical acoustic period was divided into ten phases, and a custom Matlab code was employed to identify image pairs from different cycles, but corresponding to the same phase. At least one hundred pairs of images were acquired at each phase. This process resulted in the accuracy of the phase calculation of  $\pm 2.5^\circ$ . The instantaneous quantitative patterns of vorticity corresponding to the same phase were ensemble-averaged to produce a phase-specific flow representation that is described in detail in Section 3.2.2.

## 3. EFFECT OF RESONATOR GEOMETRY

### 3.1 Overview of acoustic response

The measured frequency and the pressure amplitude for the configuration without the splitter plate are plotted in Fig. 4 as functions of the flow velocity in the main duct. The data points shown in the plot correspond to the maximum pressure amplitude at each velocity value.

The resonance is observed to occur over three ranges of flow velocity. The frequency of the dominant resonant mode switches from the first to the fifth acoustic mode as the flow velocity  $U$  reaches approximately 31 m/s. The corresponding pressure at this point reaches 101 dB. Subsequently, the dominant frequency switches to the third mode at 39 m/s, and then to seventh acoustic mode at 43 m/s. The maximum resonance amplitude is approximately 120 dB.

The following formula that is based on linear stability analysis was used to calculate frequencies of hydrodynamic (Strouhal) modes of the shear layer oscillation.

$$f = \frac{U_c}{U} \left( n_s - \frac{1}{4} \right) \left( \frac{U}{L_{eff}} \right) \quad (3)$$

where  $f$  is the shear layer oscillation frequency,  $U$  is the mean flow velocity,  $U_c$  is the convective speed of the vortices,  $n_s$  is the hydrodynamic (Strouhal) mode number that indicates the number of vortices formed in the shear layer during a typical oscillation period, and  $L_{eff}$  is the effective (characteristic) length of the cavity. In the present investigation a value of 0.4 was used for  $U_c/U$  in the calculation of the hydrodynamic frequencies in the case without plate.

The diagonal lines labeled as  $(H_1)_L$  and  $(H_2)_L$  in Fig. 4 correspond to the calculated first and second hydrodynamic (Strouhal) modes, with  $L$  (cavity length) being the characteristic length. Both calculated hydrodynamic modes  $((H_1)_L)$  and  $((H_2)_L)$  provide a good fit to the measured frequencies.

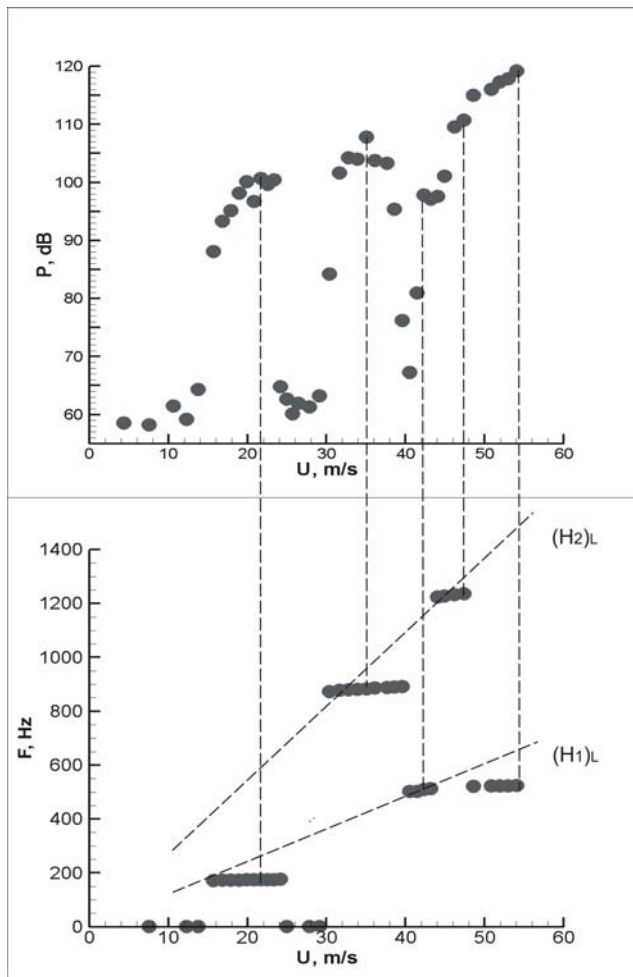


**FIG. 4 PRESSURE AMPLITUDE AND FREQUENCY AS FUNCTIONS OF INFLOW VELOCITY ( $c/t=0$ )**

Considering the response of the resonator in the presence of a short splitter plate ( $c/t = 2.7$ ), it can be observed in Fig. 5 (and confirmed by flow visualization) that only the second hydrodynamic oscillation mode results in tone generation. When a splitter plate is present in the cross-junction region, the maximum pressure amplitude decreased to 115 dB. Frequencies of the hydrodynamic shear layer oscillation modes (Strouhal modes) as functions of flow velocity were

calculated using Eqn. (3) and several values of the effective cavity length ( $L_{eff} = L, L_1, L_2$ , and  $c$ , as they are defined in Fig. 2).

It should be noted that the experimental data corresponded to the hydrodynamic mode that is based on  $L_{eff} = L$  ( $(H_2)_L$ ) and  $U_c/U = 0.6$ , while hydrodynamic modes that were calculated using the values of  $L_{eff} = L_1$ ,  $L_{eff} = L_2$  and  $L_{eff} = c$  ( $(H_2)_{L1}$ ,  $(H_2)_{L2}$  and  $(H_2)_c$ ) over-predicted the experimental data for various values of convective speed. Relatively high values of convective speeds ( $0.6U$ ) are attributed to the presence of splitter plate and the consequent need to satisfy momentum balance. Although, frequencies that were calculated based on  $L_{eff} = L_1$  matched the experimental data with a low convective velocity when first hydrodynamic mode was used, there was no evidence of the first hydrodynamic oscillation mode obtained from the flow patterns (Section 3.2), which further stresses the importance of flow visualization.

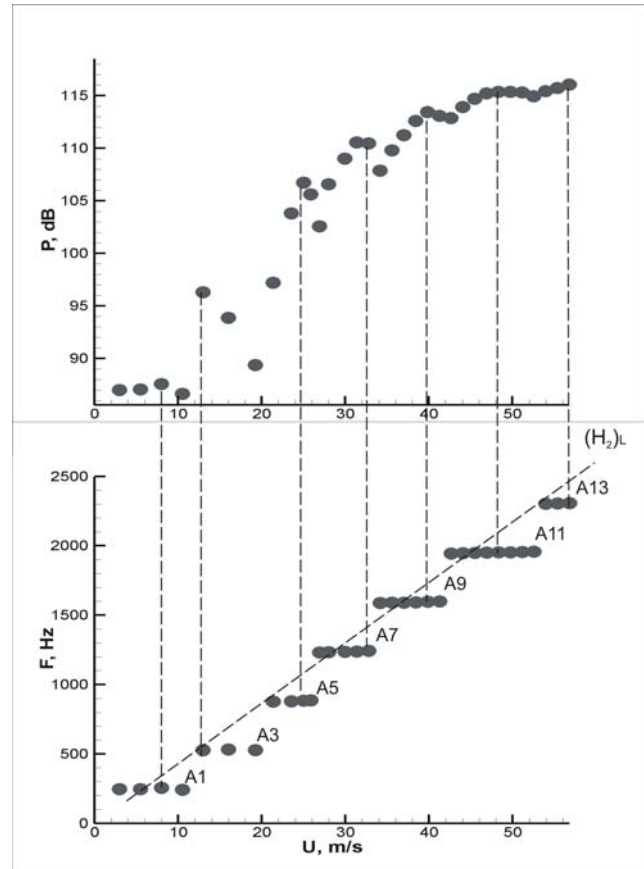


**FIG. 5 PRESSURE AMPLITUDE AND FREQUENCY AS FUNCTIONS OF INFLOW VELOCITY ( $c/t=2.7$ )**

In the case of a long splitter plate ( $c/t = 5.4$ ) shown in Fig. 6, the data trend remained qualitatively similar to the case of  $c/t = 2.7$ . The Strouhal (hydrodynamic) mode of the shear layer oscillation also corresponded to a characteristic length  $L_{eff} = L$ . The maximum pressure amplitude further decreased to 112 dB.

In general, for all three cases, the best correspondence between the calculated Strouhal mode and the experimental data was obtained when the distance between the upstream and the downstream edges ( $L_{eff} = L$ ) was utilized for evaluation of the hydrodynamic shear layer frequencies. It should also be noted that the presence of the splitter plate did not significantly affect the theoretically predicted acoustic modes of the system, while hydrodynamic features were

significantly affected. As a result, the first hydrodynamic mode was suppressed and the maximum pressure decreased, which can be explained as follows. Generation of vorticity around the splitter plate affected the amount of energy that was transferred between the vorticity-bearing flow and the resonant acoustic field. Therefore, the maximum values of acoustic pressure decreased as the splitter plate length was increased. Also, it should be noted that the absence of the first hydrodynamic mode in the case involving the splitter plates led to the decrease of 5-9db in the maximum acoustic pressure observed in the present study.

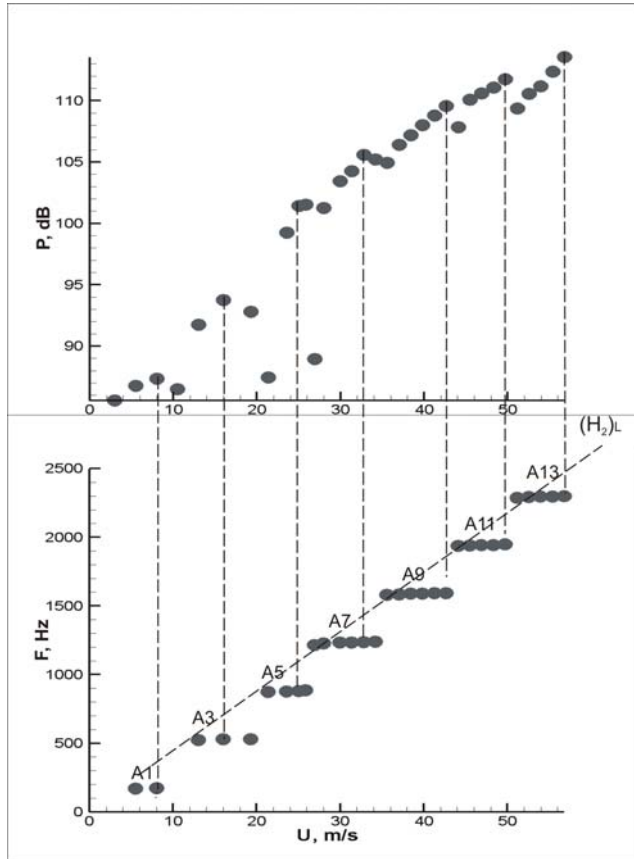


FIG. 6 PRESSURE AMPLITUDE AND FREQUENCY AS FUNCTIONS OF INFLOW VELOCITY ( $c/t=5.4$ )

### 3.2 Overview of flow patterns

#### 3.2.1 Instantaneous flow patterns

An insight into the physics of the acoustically-coupled shear layers and their interaction with the splitter plates was provided by global quantitative flow imaging using digital PIV. Figs. 7 and 8 provide an overview of the out-of-plane vorticity distribution for the cases of  $c/t = 0$ ,  $c/t = 2.7$  and  $c/t = 5.4$ , respectively.

Images presented in Fig. 7 correspond to the first and the second hydrodynamic modes of the shear layer oscillation, when one and two large-scale vortices form in the shear layers during a typical oscillation cycle, respectively. For the case of the first hydrodynamic mode, the mean inflow velocity was equal to  $U = 50$  m/s and the acoustic frequency was equal to  $f = 524$  Hz, which corresponded to a Strouhal number of  $Sr = fL/U = 0.26$ .

In the case of the second hydrodynamic mode shown in Fig. 7(b), the mean inflow velocity was equal to  $U = 31$  m/s

and the acoustic frequency was equal to  $f = 877$  Hz, which corresponded to a Strouhal number of  $Sr = fL/U = 0.72$ .

The vorticity plots illustrate formation of large-scale vortical structures in the separated shear layers. As the vortices were convected downstream along the cavity opening, their peak vorticity decreased, but the overall circulation values increased due to a larger spatial extent. Moreover, the large-scale vortices were moving across the side branch openings at higher convective speed. The vorticity plots show that the shear layer oscillation coupled with an acoustic mode drastically increased the oscillation amplitude for the case of the first hydrodynamic mode, while in the case of the second mode the transverse oscillations were less pronounced.

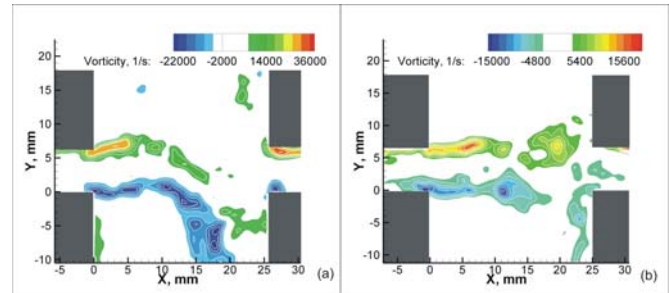


FIG. 7 PATTERNS OF INSTANTANEOUS VORTICITY CORRESPONDING TO THE FIRST (a) ( $Sr = 0.26$ ) AND THE SECOND (b) ( $Sr = 0.72$ ) HYDRODYNAMIC MODES FOR THE CASE OF  $c/t = 0$

The cases involving the splitter plates are presented in Fig. 8 for  $c/t = 2.7$  and  $c/t = 5.4$ . These flow patterns correspond to the second hydrodynamic mode of the shear layer oscillation, which is consistent with the acoustic response of the resonator. The mean flow velocity in these cases was equal to  $U = 28$  m/s and the acoustic frequency was equal to  $f = 877$  Hz, corresponding to a Strouhal number of  $Sr = fL/U = 0.78$ . The presence of the splitter plates significantly affected the dynamics of the shear layers along the entire span of side branches. Hydrodynamic interaction between the vortices in the upper and lower shear layers was limited, while the flow separation at the leading edge of the splitter plate significantly altered the flow patterns by deflecting the path of the shed vortices.

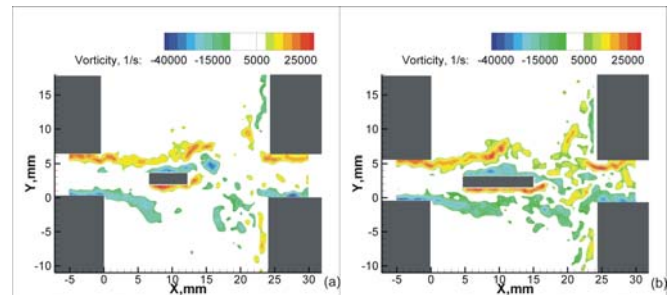
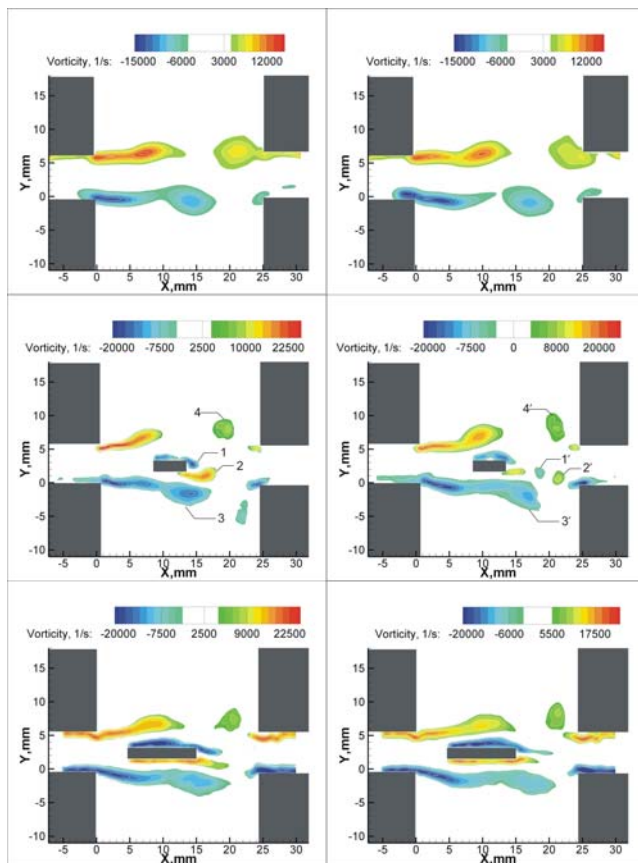


FIG. 8 PATTERNS OF INSTANTANEOUS VORTICITY FOR THE CASE OF  $c/t = 2.7$  (a) AND  $c/t = 5.4$  (b).  $Sr = 0.78$

For the case of  $c/t = 2.7$ , it can be seen in Fig 8(a) that the shear layers formed at the leading edge of the plate and reattached in the vicinity of the trailing edge, which corresponded to regime (2) described in Section 1.2. The flow pattern of Fig. 8(b) shows formation of the separation bubble along the upper and lower surfaces of the splitter plate, which is consistent with regime (3). The following section describes these processes in more detail.

### 3.2.2 Phase-averaged flow patterns

In addition to the instantaneous flow measurements, analysis of the measured acoustic pressure in conjunction with PIV imaging resulted in a series of phase-averaged images that illustrates formation and propagation of large-scale vortices during a typical acoustic cycle. Figs. 9 and 10 show the phase-averaged flow patterns for the three values of the splitter plate chord length at two phases  $\phi$  of the acoustic cycle. These flow patterns were obtained by ensemble-averaging of up to 100 PIV images that were acquired at the same phase of the acoustic pressure oscillation cycle. In the present study,  $\phi = 0^\circ$  corresponded to the instant when the acoustic velocity in the cross-junction changed sign from negative to positive. The left and the right columns of Fig. 9 correspond to  $\phi = 36^\circ$  and  $\phi = 144^\circ$ , respectively. At these phases, the acoustic velocity was directed into the upper side branch, and a new vortex formed at the upstream edge of the upper side branch. The vortex in the lower shear layer had been fully developed and convected downstream. The top, middle and bottom rows of Fig. 9 correspond to the cases of  $c/t = 0$ ,  $c/t = 2.7$  and  $c/t = 5.4$ , respectively. It should be noted that all cases presented in Fig. 9 correspond to the second hydrodynamic mode.



**FIG. 9 PATTERNS OF PHASE-AVERAGED VORTICITY CORRESPONDING TO THE CASES OF  $c/t=0$ , 2.7 AND 5.4 AT  $\phi = 36^\circ$  AND  $\phi = 144^\circ$**

Considering the case of  $c/t = 2.7$ , it can be seen in the left-middle plot of Fig. 9 that the interaction of the shear layers with the splitter plate resulted in the enhanced transverse oscillation of the upper shear layer. The amplitude of this oscillation is directly related to the generated acoustic power. Farther downstream, flow separation at the leading edges of the splitter plate resulted in formation of two

additional shear layers, which interacted with the trailing edge of the plate and subsequently formed a vortex street in the wake of the plate. The vortices that originated from the upper and the lower surfaces of the plate are labeled “1” and “2”, respectively. At  $\phi = 36^\circ$ , vortex 1 was directed downward, while vortex 2 was convected downstream with less pronounced displacement in the vertical direction. The trajectory of vortex 2 was influenced by the presence of larger vortex 3.

The trajectory of the shed vortices can be identified in the flow pattern shown in the middle-right image of Fig. 9, corresponding to  $\phi = 144^\circ$ . In this plot, a prime symbol is used to identify the vortices labeled by numbers in the plot corresponding to  $\phi = 36^\circ$ . The vortices 1' and 2' travelled toward the bottom trailing edge of the cavity with relatively higher convection speeds due to acceleration of the flow around the splitter plate. The convection speed can be approximated from the known positions of the vortices at each phase of the oscillation cycle. It should be noticed that both the shear layers that originated from the upstream edges of the side branches and those that originated from the splitter plate exhibited the second hydrodynamic oscillation mode, i.e. two vortices were formed in each shear layer during a typical oscillation cycle.

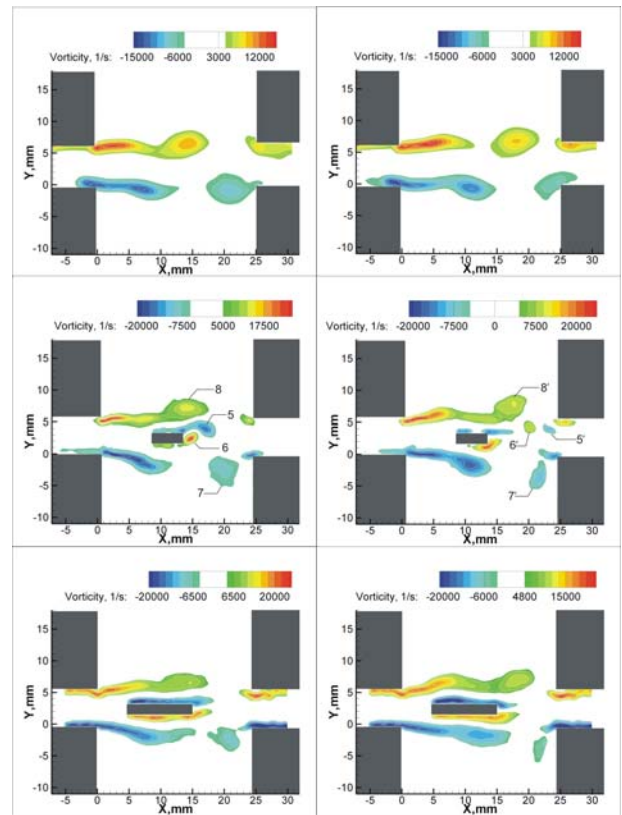


**FIG. 10 PATTERNS OF PHASE-AVERAGED VORTICITY CORRESPONDING TO THE CASES OF  $c/t=0$ , 2.7 AND 5.4 AT  $\phi = 250^\circ$  AND  $\phi = 324^\circ$**

The flow patterns corresponding to the case of  $c/t = 5.4$  are shown in the bottom row of Fig. 9. The amplitude of the oscillation of the shear layers decreased relative to the case of  $c/t = 2.7$ , and the vortex dynamics was qualitatively similar to the case of  $c/t = 0$ . In contrast to the case of  $c/t = 2.7$ , the separated shear layers reattached to the surface of the long splitter plate. This behaviour resulted in less pronounced oscillations in the wake of the plate. In addition, the vortex

street identified in the case of the short splitter plate was not observed in the case of  $c/t=5.4$ .

The left and the right columns of Fig. 10 correspond to  $\varphi = 250^\circ$  and  $\varphi = 324^\circ$ , respectively. The vortical structures formed during these phases were generally symmetric around the centerline of the duct with regard to the vortices shown in Fig. 9. During the phases shown in Fig. 10, the acoustic velocity was directed into the bottom side branch. In the case of  $c/t = 2.7$  (middle row of images), vortices 5 and 6 were shed from the splitter plate and convected toward the downstream edge of the upper side branch. The shear layers at the trailing edge of the long splitter plate ( $c/t=5.4$ , shown in the bottom row of images) were also deflected upward.

### 3.2.3 Time-averaged flow patterns

Figure 11 shows time-averaged velocity profiles corresponding to the first and the second hydrodynamic oscillation modes without a splitter plate (plots (a) and (b), respectively) as well as the second hydrodynamic mode with a splitter plate (plots (c) and (d)).

The velocity profiles presented in Fig. 11(a) correspond to the first hydrodynamic oscillation mode and exhibit significant entrainment of the fluid from the side branches into the core of the fast-moving jet, which was formed in the cross-junction region by the fluid emerging from the main duct. This entrainment resulted in a high growth rate of the jet, which can be quantified by the distribution of the vorticity thickness across the side branch opening, that is presented in Fig. 12. The velocity profiles corresponding to the second hydrodynamic oscillation mode shown in Fig. 11(b), (c) and (d) exhibited a lower spread rate of the jet.

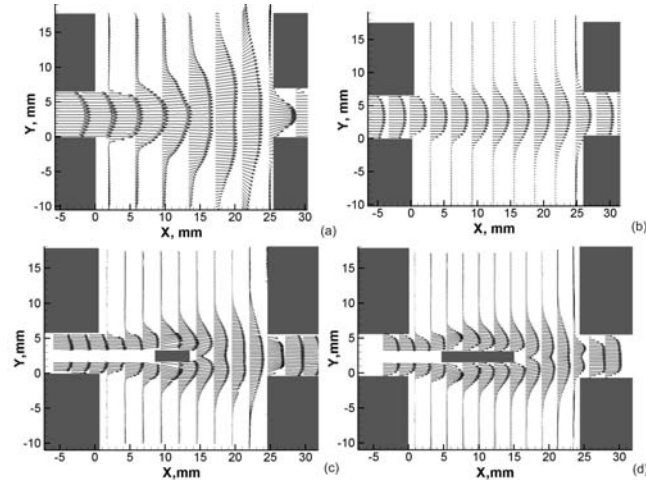


**FIG. 11 TIME-AVERAGED VELOCITY CORRESPONDING TO THE FIRST (a) AND SECOND (b) HYDRODYNAMIC MODES FOR  $c/t=0$  AND TO THE SECOND HYDRODYNAMIC MODE FOR  $c/t=2.7$  (c) AND  $c/t=5.4$  (d)**

For the cases involving splitter plates (shown in Fig. 11 (c) and (d)) the reattachment length  $X_r$  was determined from the time-averaged velocity field by calculating the location of the stagnation points on the upper and the lower surfaces of the splitter plate. The velocity vector field had a physical resolution of  $175 \times 175 \mu\text{m}^2$ , which corresponded to the uncertainty of approximately  $0.2t$  in the calculated reattachment length. For the case of the short plate ( $c/t=2.7$ ), the flow reattached to the plate at its trailing edge. For the long splitter plate ( $c/t=5.4$ ), the flow reattached upstream of the trailing edge at  $X_r/t=3.1$ . The findings of Parker et al. [20] predict larger values of the reattachment length, as

summarized in Section 1.2. This discrepancy can be attributed to the decrease of the reattachment length that was reported for the case of a turbulent inflow [17]. In addition, the reattachment length is expected to decrease when substantial blockage of the flow is present [15].

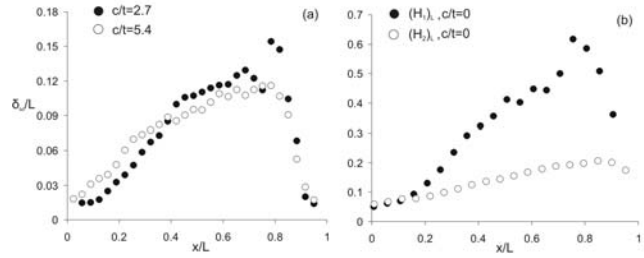


**FIG. 12 DISTRIBUTION OF VORTICITY THICKNESS ACROSS THE SIDE BRANCH OPENING FOR  $c/t=2.7$  AND  $c/t=5.4$  (a) AND  $c/t=0$  (b)**

Development of the separated shear layers, which is related to the transformation from the small-scale vortices to the large-scale clusters of vorticity, can be quantified in terms of variation of vorticity thickness as a function of the downstream distance. The vorticity thickness is defined as follows:

$$\delta_\omega = \frac{U_1 - U_2}{(\partial \langle u \rangle / \partial y)_{\max}}, \quad (4)$$

where  $U_1$  and  $U_2$  are the equivalents of the free-stream velocity on the upper and the lower sides of the shear layer. The distribution of the normalized vorticity thickness corresponding to the lower shear layer across the side branch opening is shown in Fig. 12. The filled and the open symbols correspond to the cases of  $c/t=2.7$  and  $c/t=5.4$ , respectively, in Fig. 12(a) and to the first and the second hydrodynamic oscillation modes, respectively, for the case of  $c/t=0$  in Fig. 12(b).

The streamwise variation of vorticity thickness shown in Fig. 12(a) can be classified into four stages. The first stage is related to the development of the separated shear layers upstream of the splitter plates. This stage corresponded to the region that extended from  $x/L=0$  to  $x/L=0.33$  for the case of the  $c/t=2.7$ . The corresponding growth rate of the shear layer was equal to  $d\delta_\omega/dx=0.22$ . For the case of  $c/t=5.4$ , the first stage corresponded to the region that extended from  $x/L=0$  to  $x/L=0.19$ . The corresponding growth rate of the shear layer was equal to  $d\delta_\omega/dx=0.14$ . These results are within the growth rate values (0.145 – 0.22) reported by Brown et al. [21] for plane mixing layers in the absence of acoustic coupling.

The second stage of the shear layer development corresponded to the region from  $x/L=0.33$  to  $x/L=0.42$  for the case of  $c/t=2.7$  and from  $x/L=0.19$  to  $x/L=0.27$  for the case of  $c/t=5.4$ . The shear layer growth rates for the cases of  $c/t=2.7$  and  $c/t=5.4$  were equal to  $d\delta_\omega/dx=0.37$  and  $d\delta_\omega/dx=0.33$ , respectively. The increased growth rates during the second stage of the shear layer development are attributed to the interaction of the shear layers with the splitter plates.

The third stage extended to  $x/L=0.6$ , which corresponded to the location of the trailing edge of the splitter plate for the cases of  $c/t=2.7$  and  $c/t=5.4$ . The growth rates of the shear layers decreased to  $d\delta_\omega/dx=0.12$  and  $d\delta_\omega/dx=0.115$ , respectively.

Finally, the region downstream of the splitter plates was characterized by the sharp increase of velocity gradients and

the enhanced interaction between the vortices in the wake of the splitter plate, which led to the decrease of the vorticity thickness values.

For the case of  $c/t = 0$  (no splitter plate) shown in Fig. 12(b), the first hydrodynamic mode of the shear layer oscillation  $((H_1)_L)$  corresponded to the growth rate of  $d\delta_w/dx = 0.9$ . The wavelength and scale of the vortices in the shear layer increase as the vorticity thickness increases [22]. Therefore, the plot of Fig. 12 indicates that small-scale vortices were forming in the vicinity of the upstream corner of the side branch, and that they subsequently transformed into large-scale structures at locations well downstream from the flow separation point. It should be noted that the rate of growth of the vorticity thickness abruptly increased at the downstream distance of  $x/L \approx 0.15$ . Instantaneous and phase-averaged flow patterns shown in Figs. 7-10 indicate that vortex roll-up occurred at this location. High value of the growth rate observed in the present experiments is attributed to the presence of flow-acoustic coupling, which promotes formation of large-scale vortical structures.

Figure 12(b) also shows the distribution of the normalized vorticity thickness across the lower side branch opening for the case of the second hydrodynamic oscillation mode. The vorticity thickness distribution was qualitatively similar to that observed in the case of the first hydrodynamic mode, i.e. it increased with the downstream distance. The growth rate of the shear layer across the entire cavity was equal to  $d\delta_w/dx = 0.16$ , which is substantially lower compared to the case of the first hydrodynamic mode.

In summary, the presence of the splitter plate inhibited formation of the first hydrodynamic oscillation mode and therefore substantially decreased the growth rate of the shear layers. The growth rate was found to be lower in the case of a long splitter plate ( $c/t = 5.4$ ) compared to the case of  $c/t = 2.7$ .

### 3.3 Time-averaged distribution of the acoustic source

The instantaneous acoustic power  $P_w$  generated by vorticity  $\underline{\omega}$  within a volume  $\mathfrak{R}$  can be obtained from

$$P_w = -\iiint_{\mathfrak{R}} \rho_0 (\underline{\omega} \times \underline{V}) \cdot \underline{u}_{ac} d\mathfrak{R}, \quad (5)$$

where  $\underline{V}$  is the fluid velocity, and  $\underline{u}_{ac}$  is the acoustic particle velocity. The theoretical framework for acoustic power calculation has been developed by Howe [23]. The hydrodynamic contribution to the acoustic power integral  $(\underline{\omega} \times \underline{V})$  was calculated based on the global phase-averaged flow measurements. The amplitudes of the horizontal and vertical components of the acoustic particle velocity  $\underline{u}_{ac}$  were determined using an in-house numerical model [24].

Figure 13 shows the spatial distribution of the integrand of Eqn. (5) corresponding to the first and the second hydrodynamic oscillation modes for the case without a splitter plate ( $c/t = 0$ ). Substantial interaction between the shear layers resulted in formation of a single acoustic power source region close to the centerline of the main duct, as shown in Fig. 13(a). The source was accompanied by two sinks that correspond to the regions in the shear layers where vortex development takes place. It should be noted that the source region extended almost across the entire opening of the side branches. The peak values of the generated acoustic power (4000 N/s) corresponded to large-scale vortices, which extended far into the side branches during the transverse oscillations of the separated shear layers.

Spatial distribution of the acoustic source corresponding to the second hydrodynamic mode is shown in Fig. 13(b). Immediately after the separation, the amplitude of the transverse oscillations of the shear layers was limited, and two discrete source-sink pairs existed in the vicinity of the upstream corner of the junction. The two sink regions with peak values of 190 N/s were located at  $x = 4$  mm. Farther downstream, the transverse shear layer undulations increased in amplitude, and a large single sink of acoustic power was present. This sink region exhibited high levels of negative acoustic power due to the increasing circulation of the large-scale vortices. Prior to impingement on the downstream side branch corner, the two interacting shear layers produced a single large-scale source region. Flow separation from the downstream corners of the side branches correlate with the acoustic flux into the main duct and resulted in a negative contribution to the acoustic power budget.

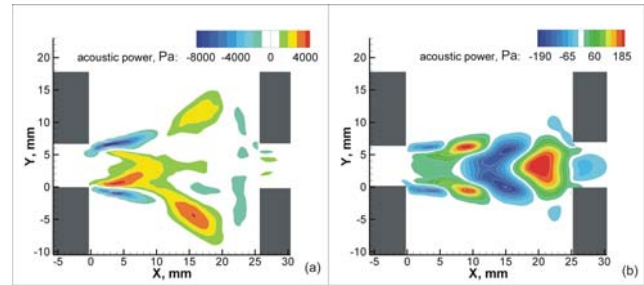


FIG. 13 TIME-AVERAGED DISTRIBUTION OF THE ACOUSTIC SOURCE CORRESPONDING TO THE FIRST (a) AND SECOND (b) HYDRODYNAMIC MODES FOR  $c/t = 0$

The time-averaged structure of the acoustic source corresponding to the cases with splitter plates is exhibited in Fig. 14.

For the case of a short plate ( $c/t = 2.7$ ) shown in Fig. 14(a), two dominant source-sink pairs extend from the leading edges of the side branches up to  $x = 15$  mm. This region corresponded to flow separation from the leading edge of the splitter plate. Additional source-sink pairs formed immediately downstream the splitter plate. Prior to impingement on the downstream corners of the side branches, interaction of the separated shear layers with the wake of the plate resulted in formation of a single large-scale source region. This region exhibited a complex structure and lower values of acoustic power compared to the two sources located in the vicinity of the plate.

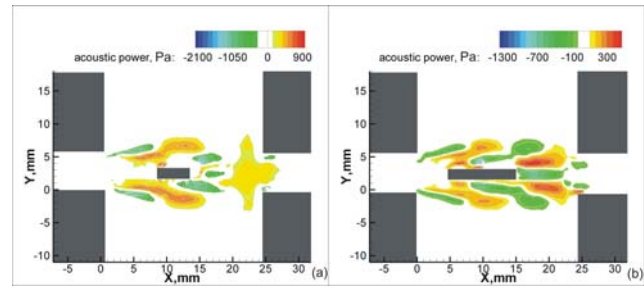


FIG. 14 TIME-AVERAGED DISTRIBUTION OF THE ACOUSTIC SOURCE FOR  $c/t = 2.7$  (a) AND  $c/t = 5.4$  (b)

In the case of the long splitter plate ( $c/t = 5.4$ ) shown in Fig. 14(b), two discrete source-sink pairs existed in the vicinity of the upstream corners of the side branches. While the sinks are similar in size and magnitude to those shown in Fig. 14(a), the source regions in the case of the long splitter

plate ( $c/t = 5.4$ ) were limited in the streamwise direction and exhibited lower values of generated power. Further downstream, two sink regions were observed in the vicinity of the splitter plate. These sinks were associated with formation of boundary layers along the horizontal surfaces of the plate. Downstream of the plate, two source regions with peak amplitude of 350 N/s were located at  $x = 20$  mm. A sink region existed between these sources in the wake of the splitter plate.

In summary, in the case of the long splitter plate ( $c/t = 5.4$ ), the peak values of the generated acoustic power substantially decreased due to the interaction of the acoustic field with the vorticity generated at the splitter plate. As a result, the amount of acoustic energy available for assisting in formation of large-scale vortical structures in the shear layers that existed across the side branches was reduced. This phenomenon is also present in large-scale industrial heat exchangers, where perforated screens and splitter plates are used for sound dissipation [11].

#### 4. CONCLUSIONS

Acoustic response of a coaxial side branch resonator with fully-turbulent inflow was investigated using a combination of digital PIV and measurements of unsteady acoustic pressure. In the case of the cross-junction without splitter plates, resonant flow tones corresponded to two hydrodynamic modes of shear layer oscillation and were characterized in terms of the acoustic pressure amplitude and the frequency of the dominant pressure peak.

In addition to the basic coaxial side branch configuration, the effects of the cross-junction geometry on the associated flow patterns were considered. Bluff rectangular splitter plates were placed along the centerline of the main duct in the vicinity of the side branch openings. This modification had a significant influence on the separating-reattaching shear layers and resulted in the attenuation of the first hydrodynamic oscillation mode, which generally decreased growth rates of the shear layers. Thus, a substantial reduction of the pulsation amplitude and of the strength of the acoustic source was observed. It should be noted that in this regard, the long plate ( $c/t = 5.4$ ) substantially outperformed the short splitter plate ( $c/t = 2.7$ ). This effect can be attributed to the difference in the flow separation and reattachment processes due to positioning of the splitter plates with respect to the upstream corners of the side branches and to the difference in the plate lengths.

In addition, the splitter plates had a pronounced effect on the spatial structure of the acoustic source due to the interaction between the unsteady shear layers that formed across the side branches and those that originated at the leading corners of the plates.

The present study provides a background to the development of noise control strategies in application to side branch systems. It should be noted, however, that deployment of splitter plate in the middle of the cross-junction is not acceptable in some applications (e.g. systems involving valves). To overcome these constraints, splitter plates can be positioned inside the main duct in the vicinity of the upstream corners of the side branches.

#### 5. REFERENCES

1. Ziada, S. and E.T. Bühlmann, *Self-excited resonances of two side-branches in close proximity*. Journal of Fluids and Structures, 1992. **6**: p. 583-601.

2. Powel, A., *Theory of Vortex Sound*. Acoustic Society of America, 1964. **36**: p. 177-195.
3. Howe, M.S., *Contributions to Theory of Aerodynamic Sound, with Application to Excess Jet Noise and Theory of Flute*. Journal of Fluid Mechanics, 1975. **71**(OCT28): p. 625-673.
4. Nelson, P.A., N.A. Halliwell, and P.E. Doak, *Fluid dynamics of a flow excited resonance. Part I: experiment*. Journal of Sound and Vibration, 1981. **78**: p. 15-38.
5. Jungowski, W.M., K.K. Botros, and W. Studzinski, *Cylindrical side-branch as tone generator*. Journal of Sound and Vibration, 1989. **131**: p. 265-285.
6. Bruggeman, J.C., et al., *Flow induced pulsations in gas transport systems: analysis of the influence of closed side branches*. ASME Journal of Fluids Engineering, 1989. **111**: p. 484-491.
7. Ziada, S., *A flow visualization study of flow-acoustic coupling at the mouth of a resonant side-branch*. Journal of Fluids and Structures, 1994. **8**: p. 391-416.
8. Kriesels, P.C., et al., *High-amplitude vortex-induced pulsations in a gas transport system*. Journal of Sound and Vibration, 1995. **184**: p. 343-368.
9. Oshkai, P. and T. Yan. *Experimental Investigation of Coaxial Side Branch Resonators*. in *ASME Pressure Vessels and Piping Division*. 2008. Vancouver, BC, Canada.
10. Velikorodny, A., T. Yan, and P. Oshkai, *Quantitative imaging of acoustically-coupled flows*. Experiments in Fluids, 2009. doi: 10.1007/s00348-009-0731-5.
11. Howe, M.S., *Attenuation of sound due to vortex shedding from a splitter plate in a mean flow duct*. Journal of Sound and Vibration, 1986. **105**(3): p. 385-396.
12. Arthurs, D., S. Ziada, and R. Bravo. *Flow Induced Acoustic Resonances of an Annular Duct with Co-Axial Side Branches* in *ASME Pressure Vessels and Piping Division Conference*. 2006. Vancouver, BC, Canada.
13. Cherry, N.J., R. Hillier, and M.E. Latour, *The unsteady structure of two-dimensional separated and reattaching flow*. Journal of Wind Engineering and Industrial Aerodynamics, 1983. **11**: p. 95-105.
14. Kiya, M. and K. Sasaki, *Structure of turbulent separation bubble*. Journal of Fluid Mechanics, 1983. **137**: p. 83-113.
15. Djilali, N. and I.S. Gartshore, *Turbulent flow around a bluff rectangular plate. Part I: Experimental investigation*. Journal of Fluids Engineering, 1991. **113**: p. 51-59.
16. Saathoff, P.J. and W.H. Melbourne, *Effects of free stream turbulence on surface pressure fluctuations in a separated bubble*. Journal of Fluid Mechanics, 1997. **337**: p. 1-24.
17. Hillier, R. and N.J. Cherry, *The effect of stream turbulence on separation bubbles*. Journal of Wind Engineering and Industrial Aerodynamics, 1981. **8**: p. 49-58.
18. Tafti, D.K. and S.P. Vanka, *A three-dimensional numerical study of flow separation and reattachment*. Physics of Fluids, 1991. **3**(12): p. 2887-2909.
19. Suksangpanomrung, A., N. Djilali, and P. Moinat, *Large eddy simulation of separated flows over a bluff plate*. International Journal of Heat and Fluid Flow, 2000. **21**: p. 655-663.

20. Parker, R. and M.C. Welsh, *Effects of sound on flow separation from blunt flat plates*. International Journal of Heat and Fluid Flow, 1983. **4**: p. 113-127.
21. Brown, G.L. and A. Roshko, *Density Effects and Large Structure in Turbulent Mixing Layers*. Journal of Fluid Mechanics, 1974. **64**: p. 775-816.
22. Monkewitz, P.A. and P. Huerre, *Influence of the Velocity Ratio on the Spatial Instability of Mixing Layers*. Physics of Fluids, 1982. **25**(7): p. 1137-1143.
23. Howe, M.S., *Contributions to the theory of aerodynamic sound, with applications to excess jet noise and the theory of the flute*. Journal of Fluid Mechanics, 1975. **71**: p. 625-673.
24. Oshkai, P., et al., *Acoustic Power Calculation in Deep Cavity Flows: A Semi-Empirical Approach*. Journal of Fluids Engineering, 2008. **130**(5).